RESEARCH ARTICLE

ADVANCED FUNCTIONAL MATERIALS
www.afm-journal.de

Promising VO_2(B)/rGO Heterojunction Cathode for Building High-Capacity and Long-Lifespan Ca-Ion Batteries

Yu Wang, Junjun Wang, Wenwei Zhang, Feiyang Chao, Jinghao Li, Qinghong Kong, Fan Qiao, Lei Zhang, Meng Huang,* and Qinyou An**

Calciumion batteries (CIBs) are an appealing energy storage technology owing to the low redox potential of Ca^{2+}/Ca and the abundant Ca reserves in the earth's crust. However, suitable cathode materials with high capacity and long lifespan are scarce. Herein, VO_2(B)/reduced graphene oxide (rGO) heterojunction formed by interfacial V—O—C bonds is constructed and first reported as a cathode material for CIBs, which exhibits an ultrahigh discharge capacity of 319.2 mAh g^{-1} and exceptional long lifespan (3000 cycles at 500 mA g^{-1} with capacity retention of 85%). In addition, VO_2(B)/rGO heterojunction also shows an outstanding rate capability at 50 °C (127.1 mAh g^{-1} at 1000 mA g^{-1}). The remarkable electrochemical performance is attributed to the big tunnel structures of VO_2(B) and the role of rGO in enhancing electronic conductivity. Density functional theory calculations reveal a feasible Ca^{2+} diffusion path at the interface. Furthermore, a reversible single-phase insertion/extraction reaction is revealed by in situ X-ray diffraction, ex situ Raman, and ex situ X-ray photoelectron spectroscopy. This work demonstrates that VO_2(B)/rGO holds great potential for building high-capacity and long-lifespan CIBs.

1. Introduction

Lithium-ion batteries (LIBs) currently dominate the commercial battery market, powering a wide range of devices from electric vehicles to portable electronics. Nevertheless, LIBs show safety concerns stemming from potential Li-dendrite and flammability of organic electrolytes, and face constraints due to the limited reserves of lithium resources. Furthermore, the technological advancements in LIBs almost reached their theoretical limits,[1] thereby emphasizing the significance of exploring alternative electrochemical energy storage systems. A number of multivalent-ion batteries, for instance, Ca-ion, Zn-ion, Mg-ion, and Al-ion batteries, have been properly proposed and methodically explored as multiple electron transfer occurs with one multivalent charge carrier migration.[2] In the group of all these multivalent-ion batteries, Ca-ion batteries (CIBs) draw wide attention because of the low redox potential of Ca^{2+}/Ca (-2.87 V vs SHE) and the low charge density of Ca^{2+} (0.49 e Å^{-3} vs 1.18 e Å^{-3} for Zn^{2+}, and 1.28 e Å^{-3} for Mg^{2+}),[3] rendering CIBs to potentially have higher working voltage and rate capabilities. Additionally, CIBs are not likely to form dendrites during electrochemical processes.[4] These merits make CIBs the most promising next-generation energy storage system for a wide range of applications with high safety, low-cost, high-energy density, and exceptional rate performance.

To date, there have been significant achievements in electrolytes that enable highly reversible calcium plating/stripping[5] and low charge transfer barriers betwixt electrode and electrolyte.[6] For instance, Zhao-Karger and co-workers[7] reported $Ca[B(hfip)_4]_2$ based electrolytes that demonstrated reversible Ca deposition at ambient temperature, which accelerated the application of CIBs. However, there hasn't been much advancement in the hunt for cathode materials that permit reversible Ca^{2+} insertion/extraction. Based on chemical compositions, the reported cathode materials for CIBs can be categorized into four groups: oxide compounds, chalcogenide compounds, Prussian blue analogs, and polyanions.[3b] Various materials, such as $Ti_2O(PO_4)_2(H_2O)$,[8] $Mg_xV_2O_5\cdot nH_2O$,[9] $V_2O_5\cdot 0.63H_2O$,[10] Zr-$NH_4V_4O_{10}$,[11] and β-$Ag_{0.33}V_2O_5$,[12] are afflicted by unsatisfied electrochemical performances, especially

Y. Wang, J. Wang, W. Zhang, F. Chao, J. Li, Q. Kong, F. Qiao, L. Zhang, Q. An
State Key Laboratory of Advanced Technology for Materials Synthesis and Processing
Wuhan University of Technology
Wuhan 430070, China
E-mail: zhanglei1990@whut.edu.cn; anqinyou86@whut.edu.cn

L. Zhang, Q. An
Hainan Institute
Wuhan University of Technology
Sanya 572000, P. R. China

M. Huang
Sanya Science and Education Innovation Park of Wuhan University of Technology
Sanya 572000, P. R. China
E-mail: 211808@whut.edu.cn

Q. An
Hubei Longzhong Laboratory
Wuhan University of Technology (Xiangyang Demonstration Zone)
Xiangyang 441000, P. R. China

The ORCID identification number(s) for the author(s) of this article can be found under https://doi.org/10.1002/adfm.202314761

DOI: 10.1002/adfm.202314761

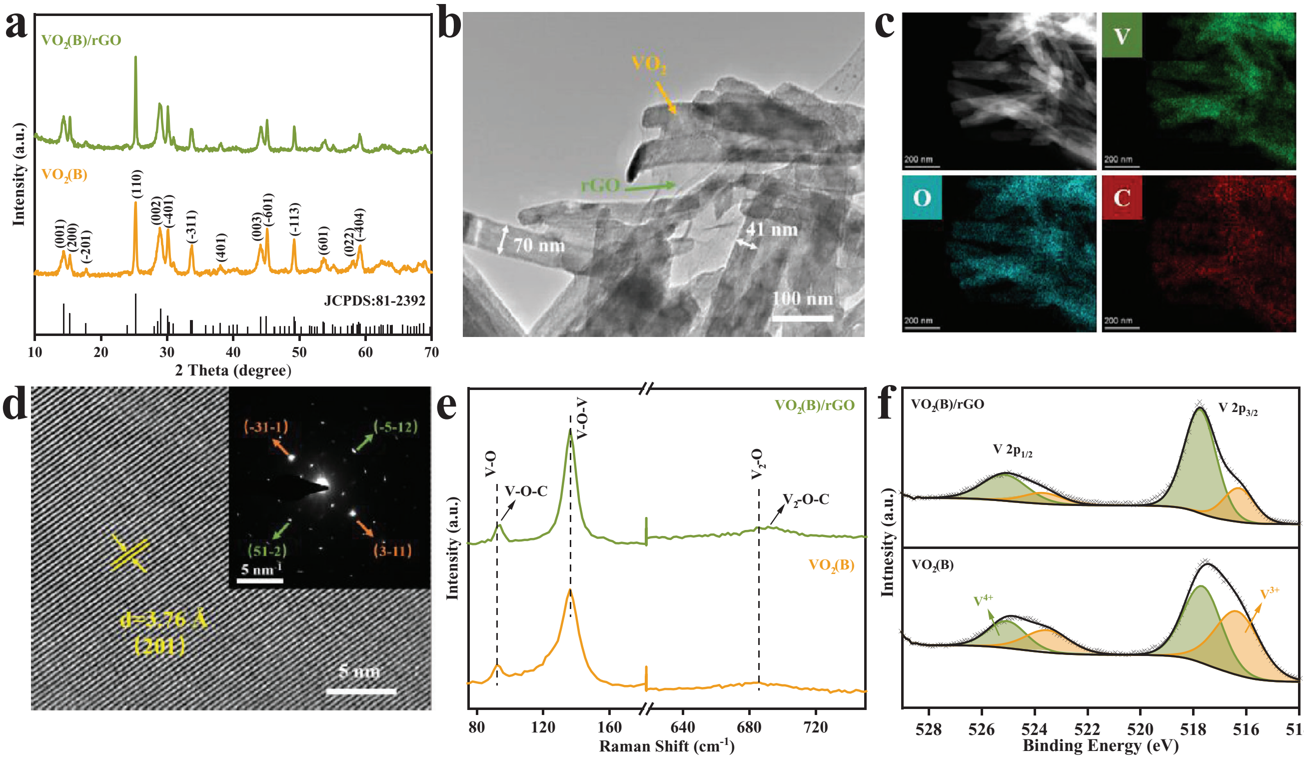

Figure 1. Structure and characterization of VO$_2$(B)/rGO. a) XRD patterns of VO$_2$(B) and VO$_2$(B)/rGO; b) TEM image and c) HAADF image and corresponding elemental maps; d) HRTEM image and the inset is SAED pattern; e) Raman spectrum of VO$_2$(B) and VO$_2$(B)/rGO; f) High-resolution XPS spectra of V 2p of VO$_2$(B) and VO$_2$(B)/rGO.

specific capacity and/or impoverished cycling performance. For example, Pyo and co-workers[8] reported $Ti_2O(PO_4)_2(H_2O)$ as a cathode material for CIBs, which shows a long cycling life of 1500 cycles. Unfortunately, the comparatively stunted capacity of 38.5 mAh g^{-1} placed restrictions on the application of this material. Hong et al.[12] reported β-$Ag_{0.33}V_2O_5$, which displays a high specific capacity of 179 mAh g^{-1} but suffers from a poor cycling life of less than 50 cycles. Thereafter, cathode alternatives with both excellent specific capacity and outstanding lifespan are highly desired for CIBs.

VO_2 exhibits different types of crystal structures, such as VO_2 (M), VO_2 (R), VO_2 (T), VO_2 (A), VO_2 (B), and VO_2 (C), etc.[13] Considering its large tunnel structures (8.2 Å^2 along the *b*-axis, 5 Å^2 along the *c*-axis, and 3.4 Å^2 along the *a*-axis),[14] metastable monoclinic VO_2(B), which shows high capacity in Zn-ion batterie (about 300 mAh g^{-1} at 100 mA g^{-1}),[15] may be a reliable cathode material for Ca^{2+} storage. Theoretically, VO_2(B) can offer a high capacity of 323 mAh g^{-1} stemming from an alterable valence state. Meanwhile, the shear-type structure of VO_2(B) can effectively mitigate the space deformation brought about by charge ions during the insertion/extraction process. Besides, although the electrochemical performances of VO_2(B) in many alkali metal batteries have been extensively investigated,[15,16] those in CIBs are still unclear. However, VO_2(B) is afflicted by the inherent defect of low electronic conductivity,[17] thereby impeding its application in energy storage. In general, the poor conductivity of electrode materials can be improved through electronic structure modulation, which typically employs three ways: doping, inducing defects, and constructing heterostructures.[18] In these ways, heterostructures typically facilitate the segregation of electrons and holes in both materials, leading to elevated electronic mobility compared to pure materials.[19] Thus, it is expected that the VO_2(B)/reduced graphene oxide (rGO) heterojunction holds significant promise as cathode materials for achieving high capacity and long lifespan in CIBs.

Herein, VO_2(B)/rGO heterojunction formed by interfacial V—O—C bonds was prepared and reported as an outstanding cathode material for CIBs. VO_2(B)/rGO exhibits an ultrahigh discharge capacity of 319.2 mAh g^{-1} and an exceptionally long lifespan (3000 times at 500 mA g^{-1} with a capacity retention of 85%), which is superior to most reported cathode materials for CIBs. In addition, VO_2(B)/rGO also shows outstanding rate capability at 50 °C (127.1 mAh g^{-1} at 1000 mA g^{-1}), which exhibits a wide temperature working range. Density functional theory (DFT) and electrochemical impedance spectroscopy (EIS) were performed to explore the role of rGO. The Ca^{2+} storage mechanism and structural evolution of VO_2(B)/rGO were fully investigated by in situ X-ray diffraction (XRD), ex situ Raman, and ex situ X-ray photoelectron spectroscopy (XPS).

2. Results and Discussion

The diffraction peaks of VO_2(B) and VO_2(B)/rGO (**Figure** 1a) are fully consistent with the monoclinic phase (JCPDS NO. 81-2392), which implies great crystallinity and impurities free. The VO_2(B) crystallizes into monoclinic crystalline phase with a space group $C\ 2/m$ (No. 12), and $a = 12.3$ Å, $b = 3.69$ Å, $c = 6.4$ Å, and $\beta = 106.1°$.[13] As shown in Figure S1 (Supporting Information), [VO_6] octahedra links together by sharing corners and edges to form a large tunnel structure (8.2 × 8.2 Å^2), which is conducive to ion storage and diffusion. Both TEM (Figure 1b) and SEM images (Figure S3, Supporting Information) indicate that VO_2(B) exhibits homogeneous nanobelt morphology with a length of 1.15 µm and an average width of 40–70 nm. The rGO flakes and VO_2(B) nanobelts entangle together tightly, building a strong electronic contact. The elemental mapping (Figure 1c) shows the uniform distribution of O, V, and C. The d distance between two adjacent lattices of VO_2(B)/rGO was measured by high-resolution TEM and the lattice spacing is 3.76 Å, belonging to the (201) plane of VO_2(B) (Figure 1d). The SAED pattern of VO_2(B)/rGO exhibits trenchant and symmetric diffraction spots that contribute to excellent crystallinity. The most prominent Raman peak, observed at 136 cm^{-1} (Figure S4, Supporting Information), corresponds to the bending vibrations of the V—O—V bond. The peak at 988 cm^{-1} is the result of the stretching vibrations of V═O bonds.[20] Since corner-sharing oxygens are shared by two pyramids, the peak at 683 cm^{-1} belongs to V_2—O stretching.[21] In Figure S4 (Supporting Information) inset, the peak at 1320 cm^{-1} reflects the disorder degree of the C atomic crystal defect, whereas the peak at 1580 cm^{-1} reflects the bond stretching of sp^2 carbons,[22] indicating the successful formation of VO_2(B)/rGO composite. The Raman spectrum in Figure 1e reveals that the peaks belonging to V—O and V_2—O shift to higher wavenumbers in VO_2(B)/rGO. This shift suggests the change in the electron state of bridging oxygen, implying the formation of the V—O—C bond and V_2—O—C bond.[23] Pair distribution function (PDF) profiles (Figure S5a,b, Supporting Information) show that the peak at 1.93 Å, corresponding to V—O bonds,[24] shifts to the right after integration with GO, which indicates the elongation of V—O bonds due to the formation of V—O—C bonds. Moreover, an enhancement at the 1.6 Å peak is observed, which is attributed to the presence of C—O bonds. In the electron paramagnetic resonance (EPR) spectrum, the g-value of VO_2(B)/rGO is largely magnified compared to that of VO_2(B), indicating a change in the spin state of vanadium's lone electron as a consequence of heterogeneous bonding (Figure S5c, Supporting Information). The altered position of the G-band indicates that the formation of heterogeneous bonds leads to electron or hole doping in GO (Figure S5d, Supporting Information).[25] Besides, it is worth noting that the I_D/I_G value of VO_2(B)/rGO is 1.45, which indicates that GO has been reduced to rGO. XPS spectrum of VO_2(B) displays peaks at 517.7 and 516.3 eV, derived from V^{4+} and V^{3+}, respectively, with a ratio of 52% to 48% (Figure 1f). The existence of V^{3+} is due to the excessive amount of reducing agent added during the material synthesis process. After compounded with GO, the ratio of V^{4+} to V^{3+} becomes 76% to 24%, which indicates the vanadium in VO_2(B) was oxidized while GO received electrons and was reduced to rGO during ultrasonication. There are three peaks in the XPS spectrum of C that correspond to O—C═O, C—O—C, and C—C, respectively (Figure S6, Supporting Information). In comparison to GO, the fractional percentage of O—C═O/C—O—C bonds in VO_2(B)/rGO was reduced, which provides further evidence that GO has been effectively reduced to rGO. Brunauer-EmmettTeller (BET) and Barret-Joyner-Halenda (BJH) measurements (Figure S7, Supporting Information) indicate that VO_2(B) has a specific surface area of 25.67 m^2 g^{-1}, while VO_2(B)/rGO exhibits a specific surface area of 24.14 m^2 g^{-1}. The mesopore size distribution of VO_2(B) is centered at 2.27 nm, while that of VO_2(B)/rGO is 2.46 nm. Pores larger than 10 nm are formed due to the stacking of nanobelts. To determine the proportion of carbon in the VO_2(B)/rGO composite, CHNS(O) Elemental Analysis was employed. The results, as shown in Table S1 (Supporting Information), revealed a carbon content of 2.6% in VO_2(B)/rGO, which is close to the 2.9% mass of GO added during the material synthesis process. In summary, the above discussions imply that the VO_2(B)/rGO heterojunction with hybrid-valence vanadium and interfacial V—O—C bonds is successfully obtained.

The Ca^{2+} storage behavior of the two samples was studied in 0.3 M $Ca(TFSI)_2$/G4 (tetraethylene glycol dimethyl ether) with activated carbon cloth (ACC) as anode (**Figure** 2a). Compared to pure VO_2(B), which has a discharge capacity of 157.2 mAh g^{-1} (Figure 2b), VO_2(B)/rGO has a markedly increased discharge capacity of 319.2 mAh g^{-1}. The addition of rGO is responsible for the noticeably increased capacity. The ex situ XPS analysis of C (Figure S9, Supporting Information) reveals the emergence of a new peak corresponding to pi → pi* shake-up satellites during discharging. This observation indicates that the pi electrons of rGO change significantly, which means rGO undergoes electrochemical reactions during the charging and discharging process.[23] It is worth noting that the capacity contributed by rGO is extremely limited,[26] which is negligible compared to the capacity of 379.9 mAh g^{-1}. The role of rGO will be extensively examined in the following sections. At various current densities (Figure 2c), VO_2(B)/rGO displays great rate capacities of 319.2, 262.2, 210.2, 168, 112.4, and 72.4 mAh g^{-1}, respectively. By contrast, VO_2(B) shows a much lower discharge capacity of 157.2, 136, 100.3, 76.3, 50.2, and 35.9 mAh g^{-1} at various conditions. In addition, when returned to 20 mA g^{-1}, VO_2(B)/rGO still maintains a capacity of 329.5 mAh g^{-1}, indicating excellent reversibility. Moreover, the VO_2(B)/rGO heterojunction exhibits enhanced capacities of 216 mAh g^{-1} at 100 mA g^{-1} (Figure 2d) and 136.2 mAh g^{-1} at 500 mA g^{-1} (Figure S10, Supporting Information). The capacity retention after 700 cycles at 100 mA g^{-1} and 3000 cycles at 500 mA g^{-1} is 83% and 85%, respectively, indicating the outstanding cycling reversibility of VO_2(B)/rGO. Besides, the Coulombic efficiency of VO_2(B)/rGO (98.76%, Figure 2d) is higher than that of VO_2(B) (96.53%). Furthermore, the electrochemical performance of the VO_2(B)/rGO electrode at 50 °C was tested, as batteries may need to work under high-temperature conditions in practical applications. As shown in Figure S11 (Supporting Information), VO_2(B)/rGO heterojunction can still deliver a discharge capacity of 127.1 mAh g^{-1} at 1000 mA g^{-1}, indicating the excellent rate capacity of VO_2(B)/rGO. Besides, VO_2(B)/rGO shows an exceptionally long lifespan of 3000 cycles at 1000 mA g^{-1} with a capacity retention of 85% (Figure 2e). The above results suggest that the VO_2(B)/rGO electrode can deliver a higher specific capacity and better rate performance than VO_2(B). In order to further prove the application potential VO_2(B)/rGO heterojunction as the electrode for CIBs, the full CIBs with Ca_xVO_2 as the anode (with pre-embedded Ca^{2+}) and polyaniline (PANI) as the cathode were assembled. The structure and characterization of as-prepared PANI are shown in Figure S12 (Supporting Information). The initial discharge capacity

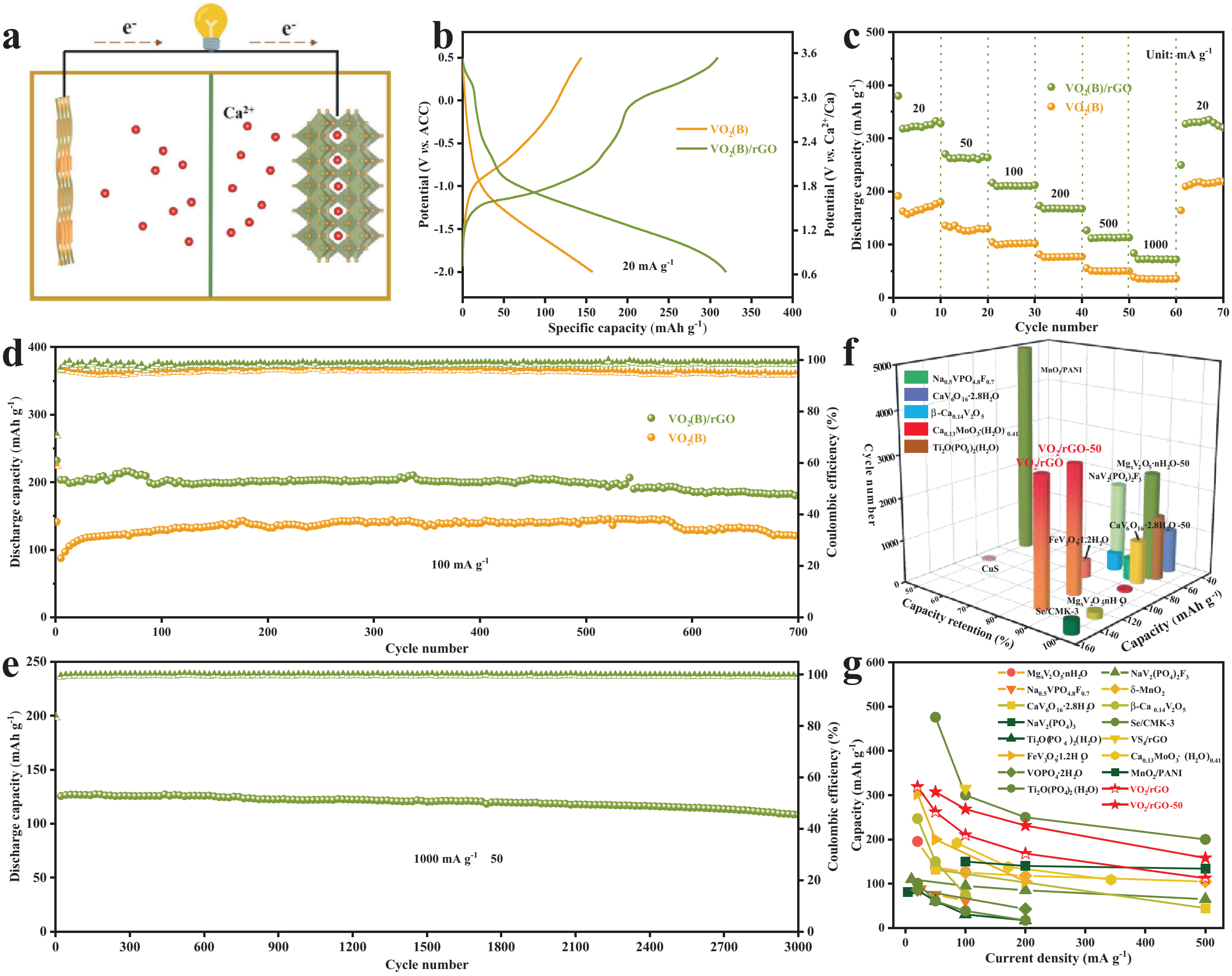

Figure 2. Calcium storage performance of VO_2(B)/rGO. a) Schematic of a rechargeable CIBs with VO_2(B) as cathode and ACC as anode; b) The galvanostatic charge/discharge profiles of VO_2(B) and VO_2(B)/rGO at 20 mA g^{-1}; c) Rate capabilities of VO_2(B) and VO_2(B)/rGO; d) Cycling performance of VO_2(B) and VO_2(B)/rGO at 100 mA g^{-1}; e) Cycling performance of VO_2(B)/rGO at 1000 mA g^{-1} and 50 °C; f,g) Comparison of the Ca^{2+} storage performance between VO_2(B)/rGO and the reported materials for CIBs in organic electrolytes.

of the full cell is 50.92 mAh g^{-1} at 20 mA g^{-1}, and it shows good reversibility, maintaining a capacity of 42.99 mAh g^{-1} after 50 cycles at 50 °C (Figure S14, Supporting Information). In addition, the comparison of the Ca^{2+} storage performance between VO_2(B)/rGO and previously reported cathode materials for CIBs, such as $Mg_xV_2O_5{\cdot}nH_2O$, $NaV_2(PO_4)_2F_3$, $Na_{0.5}VPO_{4.8}F_{0.7}$, $CaV_6O_{16}{\cdot}2.8H_2O$, δ-MnO_2, β-$Ca_{0.14}V_2O_5$, $NaV_2(PO_4)_3$[3a,9,27] are shown in Figure 2f,g. As is shown in the graph, VO_2(B)/rGO is much superior to most of the reported cathode materials for CIBs both in capacity and lifespan.

Multi-scan rate cyclic voltammetry (CV) is used to discuss the reaction kinetics of the VO_2(B)/rGO heterojunction electrode (**Figure 3a**). With the increase in scan rate, there are obvious CV peak shifts. The peak shifts can be analyzed according to Equation 1:[28]

$$i = av^b \tag{1}$$

where v is the scan rate, i is the peak current. When $b = 0.5$, diffusion dominates charge storage. When $b = 1$, it indicates capacitive controlled charge storage. The fitted b values of peak 1 and peak 2 are 0.77 and 0.83, respectively (Figure 3b), suggesting that the kinetics of Ca^{2+} storage in VO_2(B)/rGO nanobelts is jointly controlled by diffusion and capacitance. To evaluate the proportion of diffusion-controlling and capacitive-controlling, the calculation was conducted according to Equation 2:[29]

$$i = k_1 v + k_2 v^{1/2} \tag{2}$$

The capacitive-controlling contribution ratio increases from 44% to 71% (Figure 3c).[30] EIS was used to explore the reason of improved electrochemical performance of VO_2(B)/rGO heterojunction. After fitting and calculation (Figure 3d), the R_{ct} (charge transfer impedance) of VO_2(B)/rGO (15.83 Ω) is smaller than that of the VO_2(B) (28.71 Ω), proving that the rGO conductive network improves the electronic conductivity. The resistivity

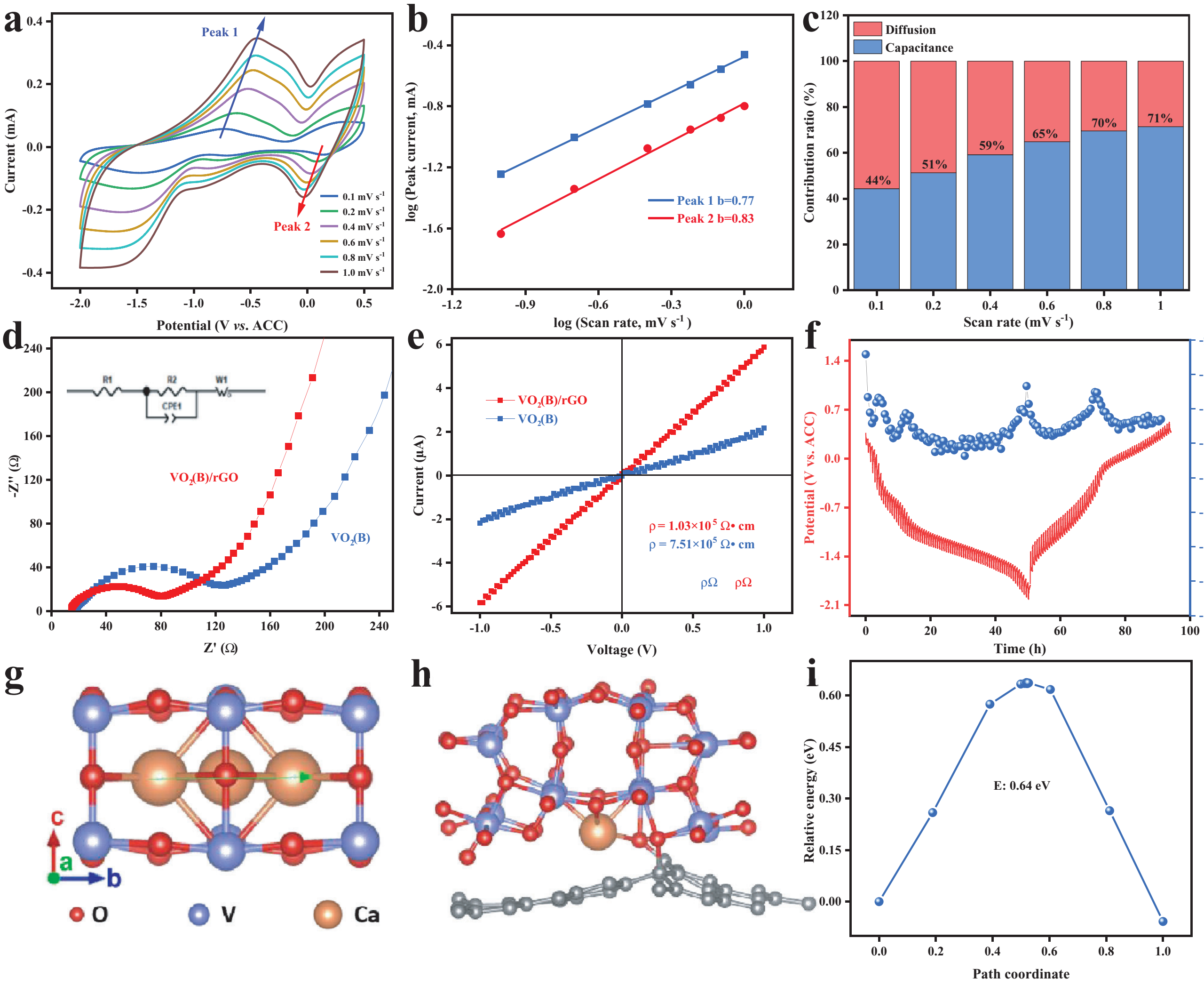

Figure 3. Reaction kinetics analysis of $VO_2(B)/rGO$. a) The CV curves of $VO_2(B)/rGO$ at different scan rates; b) Log(i) versus log(ν) plots of two redox peaks in CV curves; c) Percentage of the diffusion and capacitance contribution at different scan rates; d) EIS spectrum of $VO_2(B)$ and $VO_2(B)/rGO$ electrode, and inset is the equivalent circuit; e) Current–voltage (I–V) curves of $VO_2(B)$ and $VO_2(B)/rGO$; f) GITT curve of $VO_2(B)/rGO$ electrode and diffusivity coefficient during charge and discharge; g) Diffusion path profiles of Ca^{2+} along the b direction in $VO_2(B)$; h) Diffusion path and i) corresponding diffusion energy barrier profiles of Ca^{2+} along a direction at the interface of $VO_2(B)/rGO$.

can also be calculated by Equation 3 according to the I–V curves (Figure 3e).

$$\rho = RA/d \tag{3}$$

where A is the measured square, d is the thickness and R is the resistance. According to Equation 3, the resistivity of $VO_2(B)$ and $VO_2(B)/rGO$ was 7.51×10^5 and 1.03×10^5 Ω cm, further confirming that rGO improves the electronic conductivity. The Ca^{2+} diffusion coefficients (D^{GITT}) can be obtained based on Equation 4:[31]

$$D^{GITT} = \frac{4}{\pi\tau}\left(\frac{m_B V_M}{M_B S}\right)^2\left(\frac{\Delta E_s}{\Delta E_\tau}\right)^2 \tag{4}$$

The average D^{GITT} of Ca^{2+} in $VO_2(B)/rGO$ is 7.51×10^{-12} cm^2 s^{-1} (Figure 3f). DFT calculations suggest that Ca^{2+} can occupy the C-site (Figure 3g, Figure S15, Supporting Information) in the tunnel structure of $VO_2(B)$ with an insertion energy of -6.1 eV. Additionally, the diffusion energy barrier, obtained via climbing image nudged elastic band, of Ca^{2+} along the b-axis is 1.68 eV (Figure S16, Supporting Information), indicating the intrinsic slow diffusion kinetics in $VO_2(B)$.[32] After compounding with rGO, the diffusion energy barrier at the $VO_2(B)$ and rGO interface is merely 0.64 eV (Figure 3h,i, Figure S17, Supporting Information). The much lower energy barrier indicates a more feasible Ca^{2+} diffusion path in the interface. In summary, based on the above analysis, it can be concluded that the addition of rGO effectively enhances the electronic conductivity of the electrodes.

In order to investigate the Ca^{2+} storage mechanism and structural evolution of $VO_2(B)/rGO$, ex situ XRD, in situ XRD, ex situ

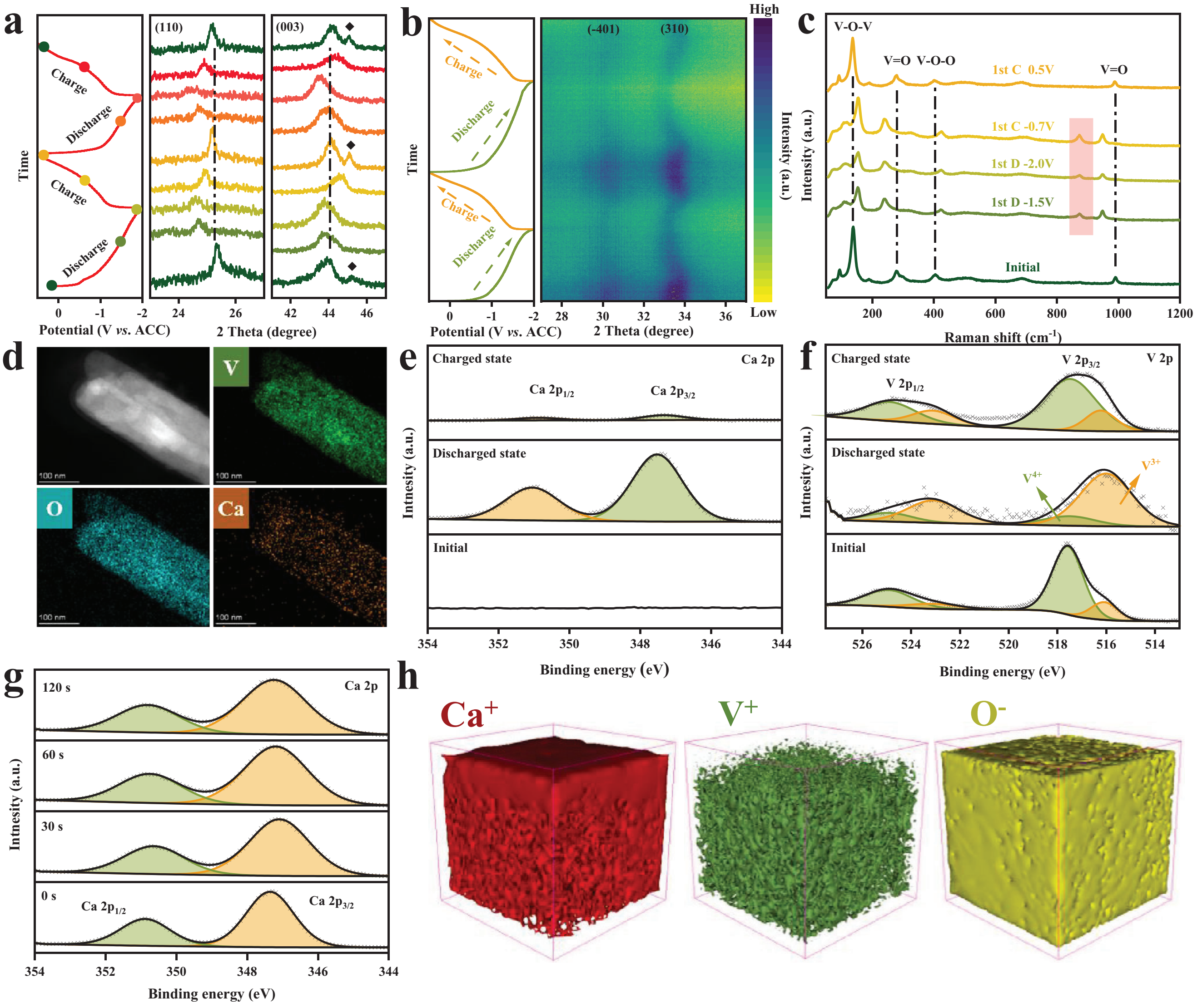

Figure 4. Calcium storage mechanism of VO_2(B)/rGO. a) Ex situ XRD patterns and b) in situ XRD patterns and the corresponding charge/discharge profiles; c) Ex situ Raman patterns of VO_2(B)/rGO electrode; d) HAADF image and corresponding elemental maps for the fully discharged VO_2(B)/rGO; Ex situ XPS spectra of e) Ca 2p and f) V 2p for VO_2(B)/rGO at different states; g) XPS etching analysis of Ca 2p; h) TOF-SIMS 3D rendering models of Ca^+, V^+, and O^- with sputter time of 600s.

Raman, and ex situ XPS were performed. Upon discharging to -2 V, the XRD peaks at 25.3°, 43.9° and 33.6° corresponding to the (110), (003) and (310) crystal plane had shifted to lower angles, suggesting that Ca^{2+} is gradually intercalated into the tunnel structures of VO_2(B) and thus expands the unit cell (**Figure** 4a,b). In contrast, when charged to 0.5 V, these peaks shift reversibly to the initial locations, demonstrating the good structural reversibility. Significantly, it is noteworthy that the patterns at the charged state exhibit more pronounced characteristics compared to those at the discharged state (Figure 4a), which is caused by the temporary irregular lattice structure induced by the insertion of Ca^{2+}. Based on XRD Rietveld refinement, the corresponding lattice constant evolution of VO_2(B)/rGO is shown in Figure S19 (Supporting Information). During the discharge process, both *b*-value and volume increase, with a maximum volume expansion of 0.6%. However, *a*-value, *c*-value, and β decrease. During charging, as Ca^{2+} are extracted, cell parameters shrink as a whole. Both in situ XRD and ex situ XRD indicate that the Ca^{2+} storage mechanism of VO_2(B)/rGO is a single-phase solid-solution reaction. Figure 4c shows the ex situ Raman spectra of the VO_2(B)/rGO electrode at the first cycle. During the discharge process, two Raman peaks at 270 and 1013 cm^{-1} shift to lower wavenumbers, and shift reversely back to the original positions during the Ca^{2+} extraction process. The low-wavenumber peaks at 163 cm^{-1} and 400 cm^{-1} show the opposite periodic shift to the above two peaks.[33] A new peak in 876 cm^{-1} appears, which is probably derived from the formation of stretching vibration of O—Ca in VO_2(B)/rGO during the charge–discharge process.[34] The HAADF images and elemental maps (Figure 4d) imply the insertion of Ca^{2+}, which is consistent with the result of energy dispersive X-ray spectroscopy (Figure S20, Supporting Information), wide XPS spectrum (Figure S21, Supporting Information), and inductively coupled plasma (Table S4, Supporting Information). Since Ca^{2+} has an 8.99% atomic ratio in the discharged state (Table S4, Supporting Information), 0.364 mol Ca^{2+} can be inserted into 1.0 mol VO_2(B)/rGO, giving a specific capacity of 235.28 mAh g^{-1}. In order to obtain the valance information of the host element during the electrochemical process, ex situ XPS was conducted. In contrast to the initial situation, the peak of Ca 2p emerges and has high intensity at fully discharged states, further demonstrating that Ca^{2+} were inserted into VO_2(B)/rGO (Figure 4e). At the charged state, the content of Ca becomes reduced but does not disappear, which means that residual Ca^{2+} exist in the VO_2(B)/rGO. Most of the V^{4+} is reduced to V^{3+} after discharge (Figure 4f), and V^{3+} is oxidized back to V^{4+} at the subsequent charging process. It can be concluded that the reduction of V^{4+} corresponds to the Ca^{2+} insertion, and the existence of a small amount of V^{3+} is due to the residual of inserted Ca^{2+}. The mechanism of calcium storage at 50 °C is consistent with that observed at room temperature, as demonstrated in Figure S22 (Supporting Information). To gain further information below the surface of the VO_2(B)/rGO electrode, XPS sputtering was applied. The XPS spectra of Ca 2p exhibited two peaks at 350.9 and 347.3 eV, which displayed similar intensities at various depths, suggesting a vertically homogeneous distribution of Ca^{2+} (Figure 4g). Furthermore, the time-of-flight-secondary ion mass spectrometry (TOF-SIMS) measurements conducted at the fully discharged electrode state reveal the homogeneous dispersion of V and O elements within the bulk structure (Figure 4h). The observed vigorous intensity of Ca^{2+} throughout the bulk reaffirms the profound insertion of Ca^{2+} into the VO_2(B)/rGO composite, corroborating the findings obtained from the XPS sputtering analysis. To investigate the morphological changes of VO_2(B)/rGO during the charge and discharge processes, ex situ TEM was employed. It can be observed that at the fully charged and fully discharged states, the nanobelt morphology of VO_2(B)/rGO remains unchanged (Figure S24, Supporting Information). Impressively, the crystal structure and morphology of VO_2(B)/rGO can be well preserved (Figures S25–S27, Supporting Information) even after 100 cycles, which reveals that the tunnel structure of VO_2(B)/rGO is sturdy and highly reversible during the Ca^{2+} insertion/extraction.

3. Conclusion

In summary, VO_2(B)/rGO heterojunction formed by interfacial V—O—C bonds is constructed and firstly reported as a cathode material for CIBs. VO_2(B)/rGO exhibits an ultrahigh discharge capacity of 319.2 mAh g^{-1} and an exceptionally long lifespan (3000 cycles at 500 mA g^{-1} with capacity retention of 85%), which is superior to most reported cathode materials for CIBs. In addition, VO_2(B)/rGO also shows outstanding rate capability at 50 °C (127.1 mAh g^{-1} at 1000 mA g^{-1}), which exhibits a wide temperature working range. The remarkable electrochemical performance is attributed to the big tunnel structures of VO_2(B) and the role of rGO in enhancing electronic conductivity. DFT calculations reveal a feasible Ca^{2+} diffusion path at the interface. Furthermore, the Ca^{2+} storage mechanism of VO_2(B)/rGO undergoes a reversible single-phase insertion/extraction reaction. TOF-SIMS and XPS sputtering further indicate the profound insertion of Ca^{2+} into VO_2(B)/rGO. This work demonstrates the excellent electrochemical performances of VO_2(B)/rGO for Ca^{2+} storage, which holds potential promise for advancing the practical application of CIBs.

Supporting Information

Supporting Information is available from the Wiley Online Library or from the author.

Acknowledgements

Y.W. and J.W. contributed equally to this work. This work was supported by the National Natural Science Foundation of China (52172231), the Sanya Science and Education Innovation Park of Wuhan University of Technology (2022KF0011), and the Natural Science Foundation of Hubei Province (2022CFA087).

Conflict of Interest

The authors declare no conflict of interest.

Data Availability Statement

The data that support the findings of this study are available from the corresponding author upon reasonable request.

Keywords

Ca-ion batteries, cathode, heterojunction, multivalent-ion battery, VO_2(B) nanobelts

Received: November 22, 2023
Revised: February 22, 2024

[1] M. L. Mao, T. Gao, S. Y. Hou, C. S. Wang, *Chem. Soc. Rev.* **2018**, *47*, 8804.
[2] a) Y. L. Liang, H. Dong, D. Aurbach, Y. Yao, *Nat. Energy* **2020**, *5*, 646; b) S. Zhang, T. Long, H. Z. Zhang, Q. Y. Zhao, F. Zhang, X. W. Wu, X. X. Zeng, *ChemSusChem* **2022**, *15*, 26.
[3] a) Z. L. Xu, J. Park, J. Wang, H. Moon, G. Yoon, J. Lim, Y. J. Ko, S. P. Cho, S. Y. Lee, K. Kang, *Nat. Commun.* **2021**, *12*, 9; b) B. F. Ji, H. Y. He, W. J. Yao, Y. B. Tang, *Adv. Mater.* **2021**, *33*, 21.
[4] S. D. Pu, C. Gong, X. W. Gao, Z. Y. Ning, S. X. Yang, J. J. Marie, B. Y. Liu, R. A. House, G. O. Hartley, J. Luo, P. G. Bruce, A. W. Robertson, *ACS Energy Lett.* **2020**, *5*, 2283.
[5] a) T. Jayaraman, A. P. Murthy, V. Elakkiya, S. Chandrasekaran, P. Nithyadharseni, Z. Khan, R. A. Senthil, R. Shanker, M. Raghavender, P. Kuppusami, M. Jagannathan, M. Ashokkumar, *J. Ind. Eng. Chem.* **2018**, *64*, 16; b) Z. Khan, S. O. Park, J. Yang, S. Park, R. Shanker, H. K. Song, Y. Kim, S. K. Kwak, H. Ko, *J. Mater. Chem. A* **2018**, *6*, 24459; c) Y. Gao, Y. L. Hong, L. C. Yin, Z. T. Wu, Z. Q. Yang, M. L. Chen, Z. B. Liu, T. Ma, D. M. Sun, Z. H. Ni, X. L. Ma, H. M. Cheng, W. C. Ren, *Adv. Mater.* **2017**, *29*, 8; d) B. Senthilkumar, C. Murugesan, L. Sharma, S. Lochab, P. Barpanda, *Small Methods* **2019**, *3*, 23; e) S. A. Ansari, Z. Khan, M. O. Ansari, M. H. Cho, *RSC Adv.* **2016**, *6*, 44616.

[6] Z. Zhao-Karger, Y. L. Xiu, Z. Y. Li, A. Reupert, T. Smok, M. Fichtner, *Nat. Commun.* **2022**, *13*, 3849.

[7] Z. Y. Li, O. Fuhr, M. Fichtner, Z. Zhao-Karger, *Energy Environ. Sci.* **2019**, *12*, 3496.

[8] S. J. R. Prabakar, W. B. Park, J. Y. Seo, S. P. Singh, D. Ahn, K. S. Sohn, M. Pyo, *Energy Storage Mater.* **2021**, *43*, 85.

[9] X. Zhang, X. M. Xu, B. Song, M. Y. Duan, J. S. Meng, X. P. Wang, Z. T. Xiao, L. Xu, L. Q. Mai, *Small* **2022**, *18*, 7.

[10] M. S. Chae, J. W. Heo, J. Hyoung, S. T. Hong, *ChemNanoMat* **2020**, *6*, 1049.

[11] M. Adil, A. Sarkar, S. Sau, D. Muthuraj, S. Mitra, *J. Power Sources* **2022**, *541*, 231669.

[12] J. Hyoung, J. W. Heo, B. Jeon, S.-T. Hong, *J. Mater. Chem. A* **2021**, *9*, 20776.

[13] Z. Khan, P. Singh, S. A. Ansari, S. R. Manippady, A. Jaiswal, M. Saxena, *Small* **2021**, *17*, 33.

[14] F. Cui, J. Zhao, D. Zhang, Y. Fang, F. Hu, K. Zhu, *Chem. Eng. J.* **2020**, *390*, 124118.

[15] M. Huang, Q. He, J. J. Wang, X. Liu, F. Y. Xiong, Y. Liu, R. T. Guo, Y. Zhao, J. L. Yang, L. Q. Mai, *Angew. Chem., -Int. Ed.* **2023**, *62*, 14.

[16] a) D. L. Chao, C. R. Zhu, X. H. Xia, J. L. Liu, X. Zhang, J. Wang, P. Liang, J. Y. Lin, H. Zhang, Z. X. Shen, H. J. Fan, *Nano Lett.* **2015**, *15*, 565; b) C. J. Niu, J. S. Meng, C. H. Han, K. N. Zhao, M. Y. Yan, L. Q. Mai, *Nano Lett.* **2014**, *14*, 2873; c) C. Y. Pei, F. Y. Xiong, J. Z. Sheng, Y. M. Yin, S. S. Tan, D. D. Wang, C. H. Hang, Q. Y. An, L. Q. Mai, *ACS Appl. Mater. Interfaces* **2017**, *9*, 17061; d) L. Q. Mai, Q. L. Wei, Q. Y. An, X. C. Tian, Y. L. Zhao, X. Xu, L. Xu, L. Chang, Q. J. Zhang, *Adv. Mater.* **2013**, *25*, 2969.

[17] W. Z. Kou, J. J. Wu, Q. Zhang, Y. H. Shen, R. J. Bi, Y. H. Li, X. W. Miao, T. H. Yang, G. Yang, *J. Alloys Compd.* **2022**, *924*, 166414.

[18] Y. H. Shen, Y. L. Jiang, Z. Z. Yang, J. Dong, W. Yang, Q. Y. An, L. Q. Mai, *Adv. Sci.* **2022**, *9*, 10.

[19] H. Sun, S. Xie, Y. Li, Y. Jiang, X. Sun, B. Wang, H. Peng, *Adv. Mater.* **2016**, *28*, 8431.

[20] H. W. Wang, H. Yi, X. Chen, X. F. Wang, *J. Mater. Chem. A* **2014**, *2*, 1165.

[21] S. H. Lee, H. M. Cheong, M. J. Seong, P. Liu, C. E. Tracy, A. Mascarenhas, J. R. Pitts, S. K. Deb, *Solid State Ionics* **2003**, *165*, 111.

[22] H. B. Zhao, L. Y. Pan, S. Y. Xing, J. Luo, J. Q. Xu, *J. Power Sources* **2013**, *222*, 21.

[23] Y. H. Dai, X. B. Liao, R. H. Yu, J. H. Li, J. T. Li, S. S. Tan, P. He, Q. Y. An, Q. L. Wei, L. N. Chen, X. F. Hong, K. N. Zhao, Y. Ren, J. S. Wu, Y. Zhao, L. Q. Mai, *Adv. Mater.* **2021**, *33*, 11.

[24] M. Baldini, P. Postorino, L. Malavasi, C. Marini, K. W. Chapman, H. K. Mao, *Phys. Rev. B* **2016**, *93*, 5.

[25] J. Lee, K. S. Novoselov, H. S. Shin, *ACS Nano* **2011**, *5*, 608.

[26] X. N. Tan, J. J. Wang, S. H. Jin, Y. Wang, F. Qiao, L. Zhang, Q. Y. An, *New J. Chem.* **2023**, *47*, 8326.

[27] a) C. H. Chen, F. Y. Shi, S. S. Zhang, Y. Q. Su, Z. L. Xu, *Small* **2022**, *18*, 9; b) C. L. Zuo, F. Y. Xiong, J. J. Wang, Y. K. An, L. Zhang, Q. Y. An, *Adv. Funct. Mater.* **2022**, *32*, 8; c) J. J. Wang, J. X. Wang, Y. L. Jiang, F. Y. Xiong, S. S. Tan, F. Qiao, J. H. Chen, Q. Y. An, L. Q. Mai, *Adv. Funct. Mater.* **2022**, *32*, 8; d) S. Kim, L. Yin, M. H. Lee, P. Parajuli, L. Blanc, T. T. Fister, H. Park, B. J. Kwon, B. J. Ingram, P. Zapol, R. F. Klie, K. Kang, L. F. Nazar, S. H. Lapidus, J. T. Vaughey, *ACS Energy Lett.* **2020**, *5*, 3203; e) S. J. Richard Prabakar, A. B. Ikhe, W. B. Park, D. Ahn, K. S. Sohn, M. Pyo, *Adv. Funct. Mater.* **2023**, *33*, 29.

[28] V. Augustyn, J. Come, M. A. Lowe, J. W. Kim, P. L. Taberna, S. H. Tolbert, H. D. Abruna, P. Simon, B. Dunn, *Nat. Mater.* **2013**, *12*, 518.

[29] J. Wang, J. Polleux, J. Lim, B. Dunn, *J. Phys. Chem. C* **2007**, *111*, 14925.

[30] X. J. Pu, D. Zhao, C. L. Fu, Z. X. Chen, S. N. Cao, C. S. Wang, Y. L. Cao, *Angew. Chem., Int. Ed.* **2021**, *60*, 21310.

[31] E. Deiss, *Electrochim. Acta* **2005**, *50*, 2927.

[32] G. Henkelman, B. P. Uberuaga, H. Jonsson, *J. Chem. Phys.* **2000**, *113*, 9901.

[33] T. Y. Wei, Q. Li, G. Z. Yang, C. X. Wang, *J. Mater. Chem. A* **2018**, *6*, 8006.

[34] L. Q. Yu, S. X. Zhao, Q. L. Wu, J. W. Zhao, G. D. Wei, *Adv. Funct. Mater.* **2020**, *30*, 11.